Probing phonon-driven symmetry alterations in graphene via high-order-harmonic spectroscopy

Navdeep Rana and Gopal Dixit*
Department of Physics, Indian Institute of Technology Bombay, Powai, Mumbai 400076, India

(Received 13 June 2022; revised 21 August 2022; accepted 16 November 2022; published 28 November 2022)

High-order-harmonic spectroscopy has become an essential ingredient in probing various ultrafast electronic processes in solids with subcycle temporal resolution. Despite its immense importance, the sensitivity of high-order-harmonic spectroscopy to phonon dynamics in solids is not well known. This work addresses this critical question and demonstrates the potential of high-order-harmonic spectroscopy to probe the impact of coherent phonons on electron dynamics in solids. A pump pulse excites in-plane optical phonon modes in monolayer graphene, and a circularly polarized pulse is employed to probe the excited phonon dynamics that generates higher-order harmonics. We show that the coherent phonon dynamics alters the dynamical symmetry of graphene with the probe pulse and leads to the generation of symmetry-forbidden harmonics. Moreover, sidebands associated with the prominent harmonic peaks are generated as a result of the coherent dynamics. It is found that the symmetries and the characteristic timescale of the excited phonon mode determine the polarization and positions of these sidebands. This paper opens an avenue in time-resolved probing of phonon-driven dynamical symmetries in solids with subcycle temporal resolution.

DOI: 10.1103/PhysRevA.106.053116

I. INTRODUCTION

Vibrations of atoms within molecules and solids are fundamental processes that regulate several physical, optical, and chemical properties of matter. When light triggers atomic vibrations, atoms exhibit periodic oscillations in a particular fashion, and these light-induced vibrations could potentially lead to the modifications in various symmetries of solids. These modifications are dynamic in nature and result in several transient phenomena, such as light-induced superconductivity [1,2], vibrationally induced magnetism [3,4], and switching of electrical polarization [5], to name but a few. Thus time-resolved mapping of the interplay of lattice vibration with electronic motion on an electronic timescale is essential to comprehend several ubiquitous phenomena in solids, such as structural phase transition [6,7] and thermal [8,9] and optical properties [10–12], and to predict new concepts in solids. Several spectroscopy and imaging-based methods are employed to probe lattice vibrations in solids [13–22]. However, probing transiently evolving lattice-electronic dynamics and dynamical symmetries of solids in the presence of light in a single experimental setup is challenging. This paper addresses this crucial problem.

High-order-harmonic generation (HHG) is a nonperturbative nonlinear frequency up-conversion process and is sensitive to the subcycle electron dynamics driven by an intense laser. Over the last decade, high-order-harmonic spectroscopy became an emerging method to interrogate various equilibrium and nonequilibrium properties of solids by investigating the emitted spectrum during HHG [23–37]. In spite of the tremendous applications of high-order-harmonic spectroscopy, the impact of lattice vibration on HHG from solids remains uncharted territory, except in recent work [38,39]. This paper focuses on highlighting the abilities of high-order-harmonic spectroscopy in the time-resolved mapping of the interplay of coherent lattice vibrations and electronic motions and the time-resolved mapping of transiently evolving symmetries of solids during the dynamics.

In the following, we will demonstrate that the coherent lattice dynamics leads to the dynamical-symmetry alterations, which results in the generation of symmetry-forbidden harmonics. Moreover, coherent lattice dynamics leads to the generation of the higher-order sidebands along with the main harmonic peaks in the high-order-harmonic spectrum. The frequency and symmetry of the coherently excited phonon mode are imprinted in the position and polarization of the sidebands, respectively. The essence of our findings is presented in Fig. 1.

To illustrate the sensitivity of the coherent phonon dynamics to high-order-harmonic spectroscopy, two-dimensional graphene with $\mathbf{D}_{6h}$ point group symmetry is chosen. The phonon spectrum of graphene consists of three acoustic and three optical phonon branches. Out of the three optical phonon modes, one phonon mode is an out-of-plane mode, where the vibrations are out of the two-dimensional plane of the graphene, and the other two are in-plane modes in which lattice vibrations are confined within the plane of the graphene [40]. In-plane optical phonon modes are considered in this paper. At the Γ point, there are two degenerate in-plane optical modes with phonon frequency of 194 meV, which corresponds to a phonon oscillation period of $\simeq$21 fs [40]. These phonon modes are represented as E_{2g} or G modes and are Raman active. It is known that light can couple to a phonon mode at the Brillouin zone center and therefore the E_{2g} Raman-active

*gdixit@phy.iitb.ac.in

 ©2022 American Physical Society

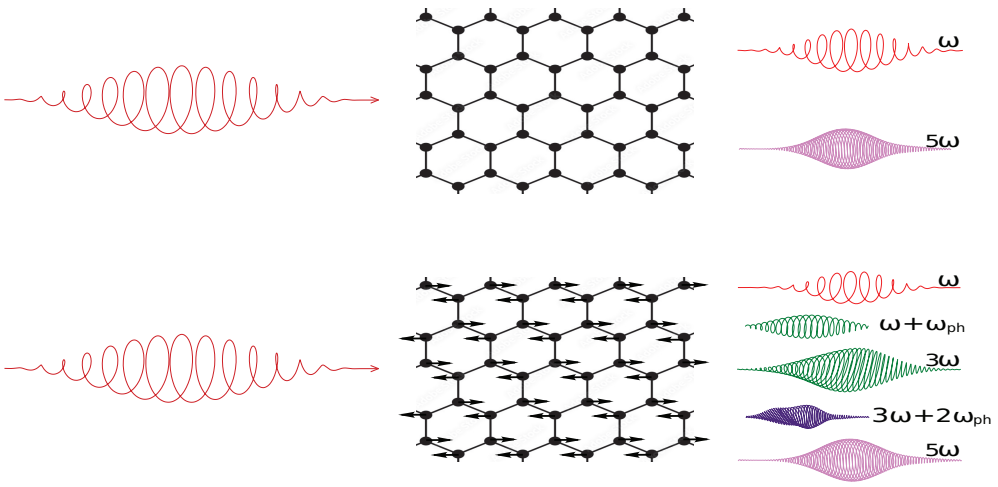

FIG. 1. Main findings of our work on the impact of coherent lattice dynamics in the high-order-harmonic spectrum of monolayer graphene.

mode can be excited by stimulated Raman excitation either via a broad pulse that covers a bandwidth of 194 meV or via two laser pulses with a difference of 194 meV in photon energy [41].

II. COMPUTATIONAL METHODS

To incorporate coherent phonon dynamics, the nearest-neighbor tight-binding Hamiltonian is extended from static to time domain as

$$\hat{\mathcal{H}}_{\mathbf{k}}(t) = -\sum_{i\in nn} \gamma_i(t) e^{i\mathbf{k}\cdot\mathbf{d}_i(t)} \hat{a}^{\dagger}_{\mathbf{k}} \hat{b}_{\mathbf{k}} + \text{H.c.} \tag{1}$$

Here, $\gamma_i(t) = \gamma_0\, e^{-(|\mathbf{d}_i(t)|-a)/\delta}$ is the time-dependent nearest-neighbor hopping energy, which is modeled to capture the temporal variations in the relative distance between nearest-neighbor atoms [$\mathbf{d}_i(0) = a = 1.42$ Å] [42,43]. $\gamma_0 = 2.7$ eV is the nearest-neighbor hopping energy, and $\delta = 0.184a_0$ is the width of the decay function with $a_0 = 2.46$ Å as the lattice parameter of the equilibrium structure [44].

Semiconductor-Bloch equations corresponding to the time-dependent Hamiltonian given in Eq. (1) are solved as

$$\frac{d}{dt}\rho^{\mathbf{k}}_{cv} = \left[-i\varepsilon_{cv}(\mathbf{k}_t, t) + \frac{1}{T_2}\right]\rho^{\mathbf{k}}_{cv} + i\mathbf{E}(t)\cdot\mathbf{d}_{cv}(\mathbf{k}_t, t)\left[\rho^{\mathbf{k}}_{vv} - \rho^{\mathbf{k}}_{cc}\right], \tag{2a}$$

$$\frac{d}{dt}\rho^{\mathbf{k}}_{vv} = i\mathbf{E}(t)\cdot\mathbf{d}_{vc}(\mathbf{k}_t, t)\rho^{\mathbf{k}}_{cv} + \text{c.c.} \tag{2b}$$

Here, the vector potential and the electric field corresponding to the driving laser field are represented as $\mathbf{A}(t)$ and $\mathbf{E}(t)$, respectively, and are related as $\mathbf{E}(t) = -d\mathbf{A}(t)/dt$. $\mathbf{d}_{cv}(\mathbf{k})$ and $\varepsilon_{cv}(\mathbf{k})$ are the dipole matrix elements and the band-gap energy between conduction and valence bands at given $\mathbf{k}$ with $\mathbf{d}_{cv}(\mathbf{k}) = i\langle c, \mathbf{k}|\nabla_{\mathbf{k}}|v, \mathbf{k}\rangle$, respectively. The time-dependent Hamiltonian in Eq. (1) is diagonalized, and dipole matrix elements are calculated during the lattice dynamics at each time step with the updated eigenstates. $\mathbf{d}_{cv}(\mathbf{k})$ becomes time dependent due to coherent phonon dynamics. The dipole matrix elements and the eigenenergies are smoothly updated in the semiconductor-Bloch equations at each consecutive time step as the displacements of the atoms and time steps are small enough [45]. To account for the interband decoherence, a phenomenological term with a constant dephasing time T_2 is introduced. Here, $\mathbf{k}_t = \mathbf{k} + \mathbf{A}(t)$.

The high-order-harmonic spectrum is calculated as

$$\mathcal{I}(\omega) = \left|\mathcal{FT}\left(\frac{d}{dt}\mathbf{J}(t)\right)\right|^2, \tag{3}$$

where $\mathcal{FT}$ stands for the Fourier transform. The total current $\mathbf{J}$(t) is calculated by integrating $\mathbf{J}(\mathbf{k}, t)$ over the entire Brillouin zone as

$$\mathbf{J}(\mathbf{k}, t) = \sum_{m,n\in\{c,v\}} \rho^{\mathbf{k}}_{mn}(t)\mathbf{p}_{nm}(\mathbf{k}_t, t), \tag{4}$$

where $\mathbf{p}_{nm}(\mathbf{k}) = \langle n, \mathbf{k}|\nabla_{\mathbf{k}}\hat{\mathcal{H}}_{\mathbf{k}}|m, \mathbf{k}\rangle$ is the momentum matrix element. The ellipticity and the phases of harmonics are estimated by following the recipe given in Ref. [46].

It is assumed that a pump-pulse initiates the coherent excitation of an in-plane Raman-active phonon mode in graphene. The excited phonon mode is probed by the high-order-harmonic generating pulse. The excitation of the phonon mode is approximated by direct initiation of the coherent vibrations of carbon atoms. Due to coherent lattice dynamics, the lattice configuration changes as a function of time. We have adopted the same methodology for HHG from a solid with phonon dynamics as given in our earlier work [45]. In the present approach, electron-phonon coupling is not included explicitly.

A circularly polarized pulse with a wavelength of 2.0 μm and peak intensity of 1×10^{11} W/cm^2 is used to generate high-order harmonics in graphene with and without coherent phonon dynamics. The pulse duration is 100 fs, which is much longer than an oscillation period of in-plane phonon dynamics $\simeq$21 fs. Moreover, the lifetime of these phonon modes is around 1 ps [47]. The parameters of the harmonic-generating laser are similar to the ones used earlier for probing electron dynamics in graphene [48].

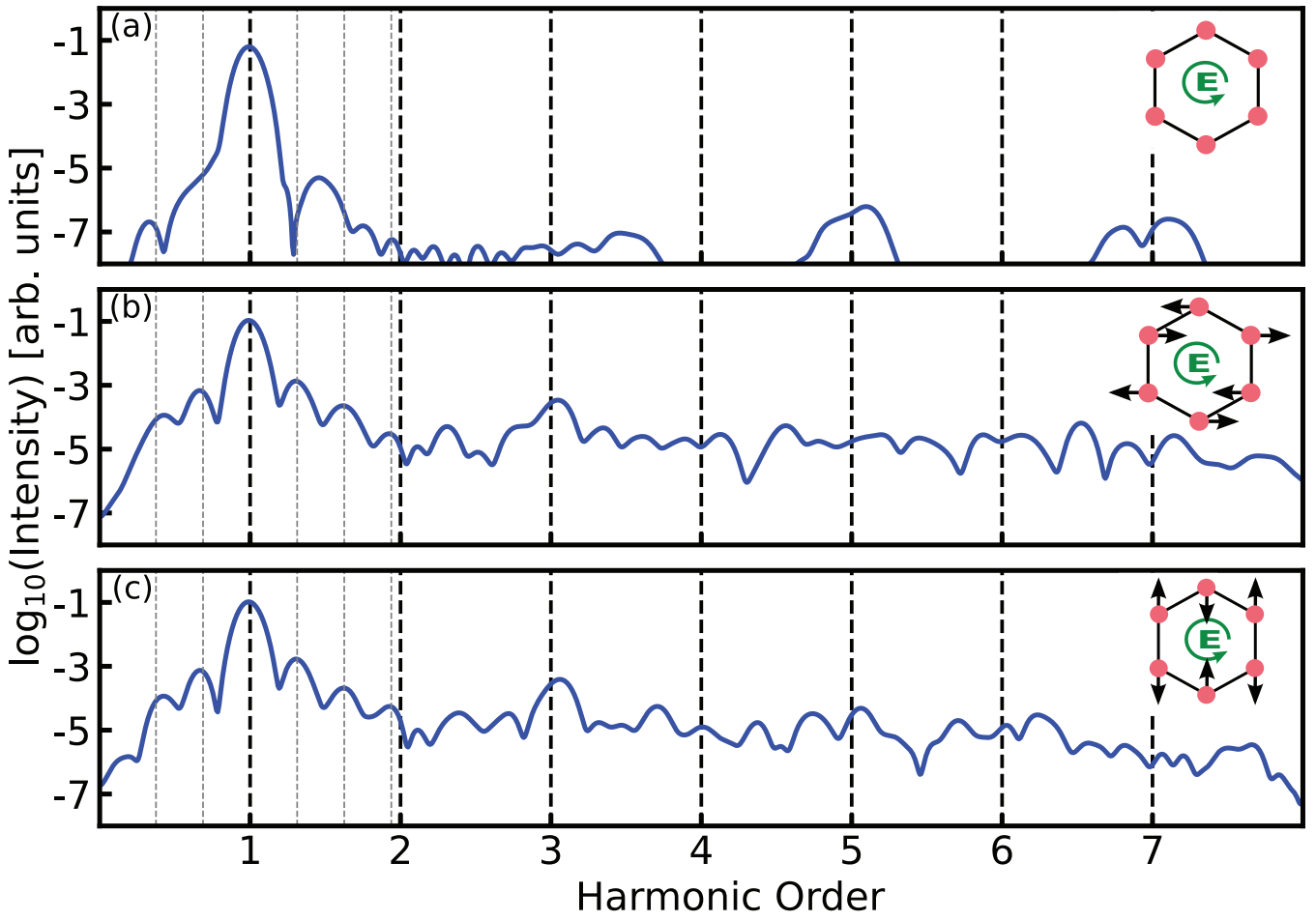

FIG. 2. High-order-harmonic spectra, generated by a left-handed circularly polarized laser pulse, of monolayer graphene with and without coherent phonon dynamics. (a) The spectra of the graphene without phonon dynamics. (b) and (c) The spectra of graphene with the coherent in-plane longitudinal optical (M_{1x}) phonon mode (b) and transverse optical (M_{2y}) phonon mode (c). In all the spectra, sidebands corresponding to the prominent harmonic peaks are identified at frequencies ($\omega_0 \pm n\omega_{\rm ph}$), where $\omega_{\rm ph}$ is the phonon frequency, ω_0 is the frequency of the probe laser pulse, and n is an integer. The unit cell of the graphene with the eigenvector of a particular phonon mode and polarization of the harmonic-generating probe pulse is shown in the respective insets. Results are presented for $T_2 = 10$ fs and a maximum $0.03a_0$ displacement of atoms from their equilibrium positions during coherent phonon dynamics, where a_0 is the lattice parameter of the equilibrium structure.

III. RESULTS AND DISCUSSION

The high-order-harmonic spectrum corresponding to monolayer graphene without phonon dynamics is presented in Fig. 2(a). We have employed a left-handed circularly polarized laser pulse for HHG in graphene with and without phonon dynamics. As dictated by the symmetry constraints and selection rules, it is expected that the circularly polarized pulse yields $(6m \pm 1)$ orders of harmonics from inversion-symmetric graphene with sixfold symmetry [49–51]. Here, $m = 0, 1, 2, \ldots$ is a positive integer. In this case, the third harmonic is symmetry forbidden. On the other hand, a linearly polarized laser pulse leads to $(2m + 1)$ orders of harmonics as shown earlier [52]. Our results shown in Fig. 2(a) are consistent with the selection rules and earlier reports [49,50]. Graphene is not chiral in nature, so left- and right-handed circular laser pulses yield the same harmonic spectra.

After discussing HHG from graphene without phonon dynamics, let us investigate how the in-plane phonon modes affect the harmonic spectrum shown in Fig. 2(a). For this purpose, we coherently excite one of the two degenerate in-plane phonon modes and assume that the excitation is done prior to the probe harmonic pulse. Figure 2(b) presents the harmonic spectrum corresponding to coherently excited phonon mode 1 (M_{1x}), in which atoms are vibrating along the X direction. The spectrum in Fig. 2(b) is drastically different from the one without phonon dynamics [see Fig. 2(a)]. There are only odd harmonics in the spectrum as the M_{1x} phonon mode preserves the inversion symmetry in graphene [45]. Moreover, the spectrum exhibits multiple sidebands along with the main odd harmonics as evident from Fig. 2(b). Our findings remain qualitatively the same for the amplitude of the lattice displacement ranging from $0.01a_0$ to $0.05a_0$ with respect to the equilibrium positions as evident from Fig. 3(a). As expected, the intensity of the sidebands increases as the amplitude of vibration increases. Moreover, the dephasing time T_2 does not impact our findings significantly as the spectra are qualitatively the same for T_2 ranging from 5 to 30 fs [see Fig. 3(b)]. The appearance of the phonon sidebands in the angle-resolved

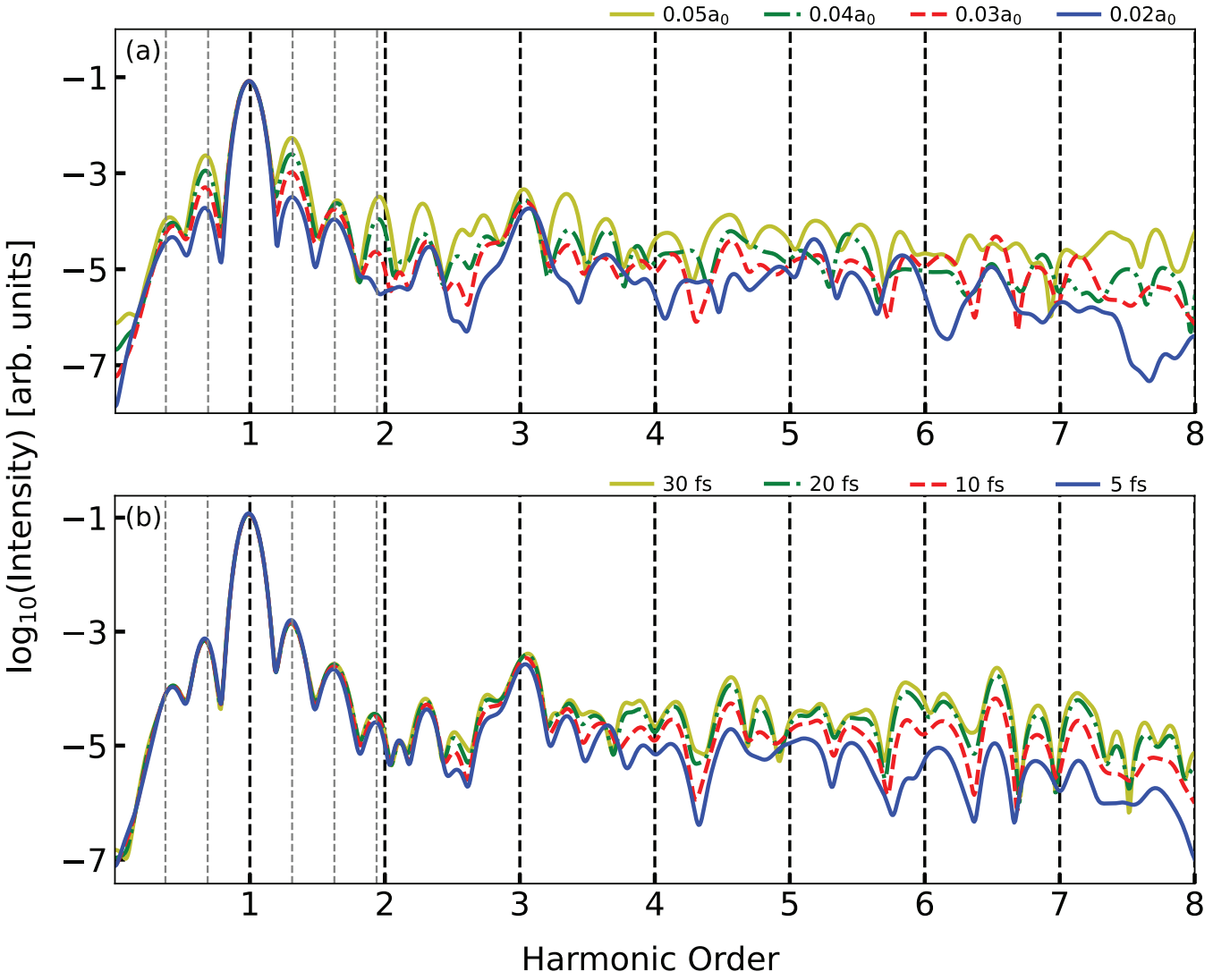

FIG. 3. High-order-harmonic spectra of graphene with the M_{1x} phonon mode for different (a) amplitudes of the atomic displacement and (b) dephasing time T_2.

photoemission spectrum of monolayer graphene within the Floquet formalism was discussed in Ref. [53].

The coherent excitation of in-plane phonon mode 2 (M_{2y}), in which atoms are vibrating along the Y direction, also leads to multiple sidebands along with the odd harmonics as visible from Fig. 2(c). In both cases, the energy separation between the successive sidebands is equal to the energy of the excited phonon (M_{1x} or M_{2y}) mode, i.e., 194 meV. Therefore the energy of the excited phonon mode is encoded in the spectra. Apparently, it seems that the spectra are insensitive to the symmetry of the excited phonon mode as both M_{1x} and M_{2y} phonon modes yield similar harmonic spectra [see Figs. 2(b) and 2(c)]. In the following, we will show that this is not the case and the symmetry of the excited phonon mode is encoded in the polarization properties of the spectra.

Not only does the coherent phonon dynamics lead to the generation of multiple sidebands, but also the forbidden harmonics become allowed. As stated earlier, the third harmonic is absent for the circular-laser-driven HHG from graphene without phonon dynamics [see Fig. 2(a)]. However, the dynamics of the coherent E_{2g} phonon mode reduces graphene's sixfold symmetry into twofold dynamically, which allows the generation of $(2m \pm 1)$ harmonic orders. The presence of the third harmonic in both cases, graphene with the M_{1x} phonon mode or graphene with the M_{2y} phonon mode, is a signature of the dynamical symmetry reduction as evident from Figs. 2(b) and 2(c). At a glance, it seems that the criteria for HHG is the same for the linearly polarized laser pulse [$(2m + 1)$ orders and third harmonic] and the combination of the phonon-driven symmetry reduction with the circularly polarized laser pulse [$(2m \pm 1)$ orders and third harmonic]. To distinguish the two situations, let us analyze the polarization properties of the emitted harmonics.

Figure 4 displays the projection of the x and y components, in the time domain, corresponding to the first and fifth harmonics of the spectrum in Fig. 2(a). It is known that the polarization of a given harmonic for a material with l-fold symmetry is determined by $lm + \sigma$, where $\sigma = +1$ ($\sigma = -1$) represents the mth harmonic's polarization, which is the same as (opposite to) the helicity of the driving laser pulse [49]. It

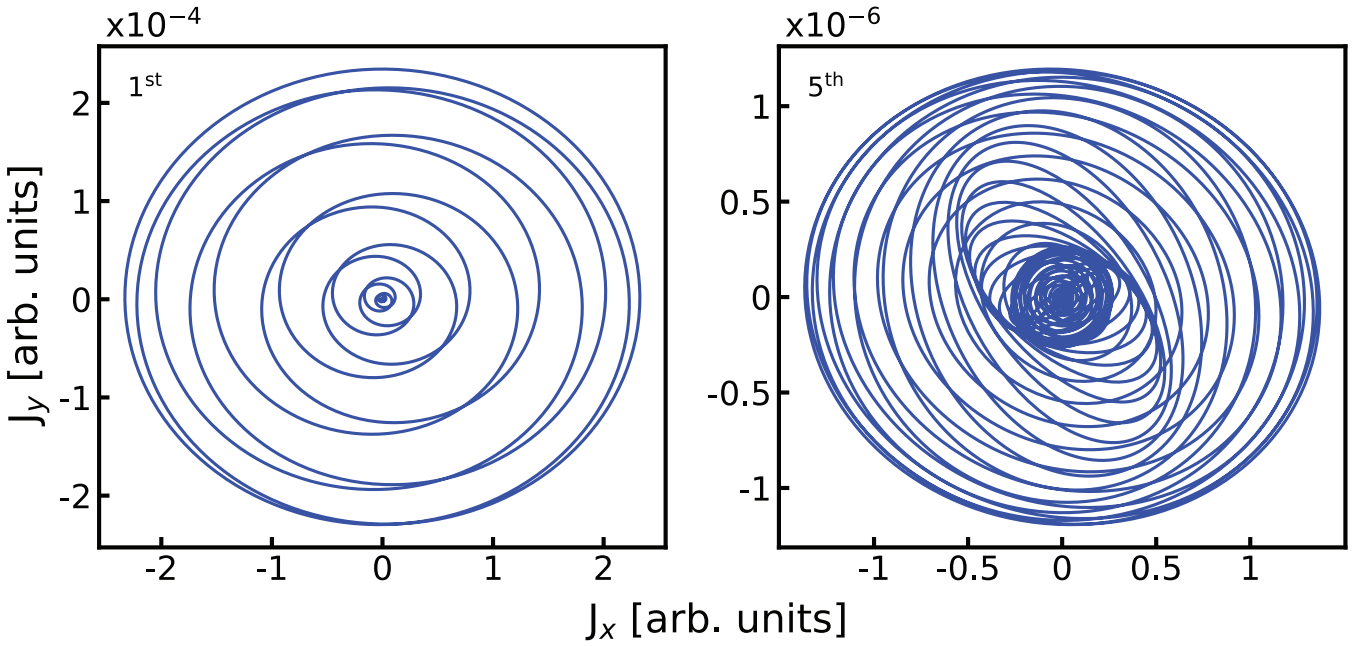

FIG. 4. The projection of the x and y components, in the time domain, of the first and the fifth harmonics corresponding to the spectrum of graphene without phonon dynamics as shown in Fig. 2(a).

is straightforward to see that the $(lm-1)$th and $(lm+1)$th harmonics are circularly polarized with $\sigma=-1$ and $\sigma=1$, respectively. In the present case, the first and fifth harmonics are circularly polarized with opposite helicity, which is consistent with earlier findings [50,54].

As stated above, $(2m\pm1)$ harmonic orders are allowed due to phonon-driven dynamical symmetry reduction from sixfold to twofold, which leads to the generation of the third harmonic. Moreover, this dynamical symmetry reduction also alters the polarization properties of the emitted harmonics. The projected x and y components of the first, third, and fifth harmonics for graphene with M_{1x} and M_{2y} phonon modes are presented in Figs. 5(a) and 5(b), respectively. As evident from the figure, the ellipticity of the first harmonic reduces drastically from 1 for graphene without phonon dynamics to 0.63 for graphene with phonon dynamics. The change in the ellipticity can be understood as follows: When the M_{1x} phonon mode is excited, carbon atoms vibrate along the X direction, which increases the velocity of the electrons in the X direction. It is known that the intraband current is proportional to the velocity, and low-order harmonics in graphene are dominated by the intraband current [52,55]. Thus the major axis of the ellipse is along the X direction in the case of the first harmonic, which reduces the ellipticity from 1 to 0.63.

Similarly, the excitation of the M_{2y} mode leads the vibrations of the atoms along the Y direction. This provides an additional velocity component to electrons in the Y direction, which translates to the major axis of the ellipse along the Y direction. The ellipticity of the fifth harmonic, corresponding to graphene without phonon dynamics to graphene with the M_{1x} (M_{2y}) phonon mode, changes significantly, i.e., from 1 to 0.93 (0.96). The phonon dynamics not only modifies the ellipticity of the harmonics significantly but also changes the phase between the x and y components of the harmonics. In the case of the M_{1x} (M_{2y}) mode, the phase differences between the components for the first and fifth harmonics are 90° (90°) and 125° (45°), respectively (see Fig. 5). The ellipticity and the phase difference of the third harmonic for graphene with the M_{1x} (M_{2y}) mode are 0.77 (0.79) and 40° (35°), respectively. Thus the changes in the ellipticity and phase indicate that the harmonics are sensitive to the symmetry of the excited phonon mode as reflected in Fig. 5.

After demonstrating how the information of the excited phonon mode and its symmetry is imprinted in the main harmonics and their polarization properties, let us analyze what information is encoded in the sidebands associated with prominent harmonics. The projection of the x and y components of the first, second, and third sidebands corresponding to the first main harmonic corresponding to graphene with the M_{1x} phonon mode is shown in Fig. 6(a). All three sidebands have nonzero x and y components as evident from the figure. The same is true for the sidebands associated with the M_{2y} phonon excitation as reflected from Fig. 6(b). Moreover, the ellipticities of the first, second, and third sidebands of the first harmonic corresponding to graphene with the M_{1x} (M_{2y}) phonon mode read as 0.98 (0.56), 0.72 (0.95), and 0.59 (0.67), respectively. Also, the phases between the x and y components of the first, second, and third sidebands of the M_{1x} (M_{2y}) mode are 85° (90°), 70° (135°), and 60° (75°), respectively. Thus the analysis of Fig. 6 establishes that the polarization and the phase properties of the sidebands are different for different phonon modes. However, it is not obvious why the sidebands have nonzero x and y components, whereas a particular phonon mode (M_{1x} or M_{2y}) induces atomic vibrations along a particular direction (X or Y).

To know the origin of the nonzero x and y components of the sidebands, we applied the Floquet formalism to graphene with a coherently excited phonon mode and circularly polarized probe pulse. The Floquet formalism determines dynamical (spatiotemporal) symmetries (DSs) of the system,

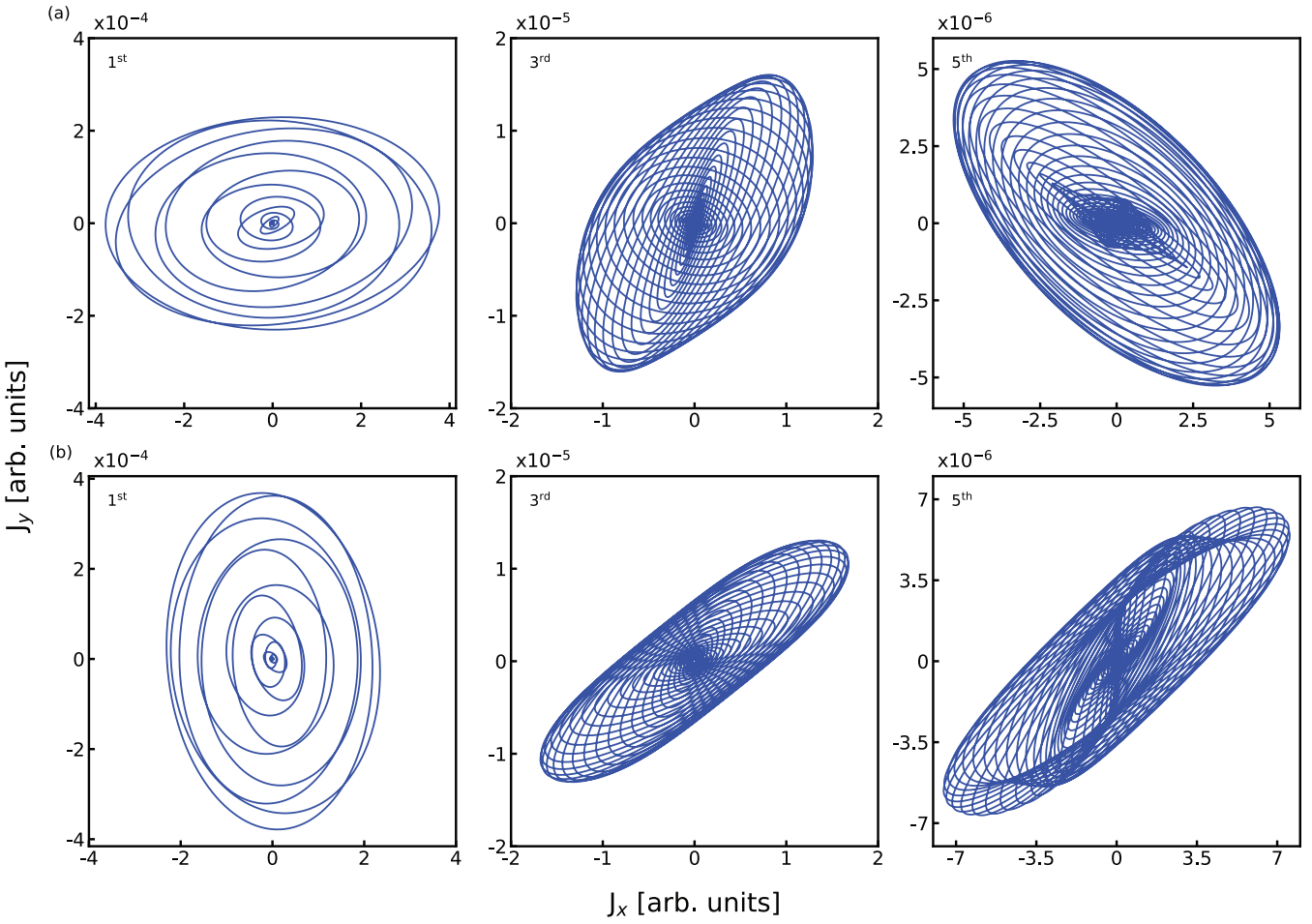

FIG. 5. Same as Fig. 4 for the first, third, and fifth harmonics for graphene with (a) M_{1x} and (b) M_{2y} phonon modes. In the case of the M_{1x} (M_{2y}) phonon mode, the ellipticities of the first, third, and fifth harmonics are 0.63 (0.62), 0.77 (0.79), and 0.93 (0.96), respectively. Also, the phase differences between the x and y components of the first, third, and fifth harmonics are 90° (90°), 40° (35°), and 125° (45°), respectively.

which dictate selection rules for the sidebands. The nth-order sideband obeys the symmetry constraint $\hat{X}^t \mathbf{E}_{s,n}(t)[\hat{X}^t \mathbf{E}(t)]^\dagger = \mathbf{E}_{s,n}\mathbf{E}(t)^\dagger$ with the condition that the spatial symmetries of $\hat{X}^t$ and the probe pulse are the same [56]. Here, $\hat{X}^t$ is a DS, and the electric fields associated with the nth-order sideband and the probe laser are represented by $\mathbf{E}_{s,n}(t)$ and $\mathbf{E}(t)$, respectively. The Raman tensor, denoted as $\mathcal{R}_n(t) = \mathbf{E}_{s,n}(t)\mathbf{E}(t)^\dagger$, has to be invariant under the operation of the DSs [56]. In the following, we will follow the same treatment as given in Refs. [45,56] to investigate the properties of the sidebands using DSs within the Floquet formalism.

In the present case, $\hat{\mathcal{D}}_1 = \hat{\sigma}_y \cdot \hat{\mathcal{T}}$ is the DS, which leaves the system with the M_{1x} phonon mode invariant. Here, $\hat{\sigma}_y$ is the reflection with respect to the y axis, and $\hat{\mathcal{T}}$ is the time-reversal operator. Thus the condition associated with the sidebands is determined as $\hat{\mathcal{D}}_1 \mathcal{R}_n(t) = \mathcal{R}_n(t)$ with

$$\mathcal{R}_n(t) = \mathbf{E}_{s,n}(t)\mathbf{E}(t)^\dagger = \begin{bmatrix} E_{s,n_x}E_x^* & E_{s,n_x}E_y^* \\ E_{s,n_y}E_x^* & E_{s,n_y}E_y^* \end{bmatrix}. \quad (5)$$

Let us substitute the expression of $\mathbf{E}(t)^\dagger = [\cos(\omega_0 t)E_x^\dagger \;\; \sin(\omega_0 t)E_y^\dagger]$, where ω_0 is the frequency of the probe pulse in the above equation; the expression of the Raman tensor reads as

$$\mathcal{R}_n(t) = \sin[(n\omega_{\rm ph} + \omega_0)t] \begin{bmatrix} \cos(\omega_0 t)E_{s,n_x} \\ \sin(\omega_0 t)E_{s,n_y} \end{bmatrix}. \quad (6)$$

Here, $\omega_{\rm ph}$ is the frequency of the phonon mode. Operating $\hat{\mathcal{D}}_1$ on $\mathcal{R}_n(t)$ leads to the following expression of the invariant $\mathcal{R}_n(t)$:

$$\sin[(m\omega_{\rm ph} + \omega_0)t] \begin{bmatrix} \cos(\omega_0 t)E_{s,n_x} \\ \sin(\omega_0 t)E_{s,n_y} \end{bmatrix} = \sin[-(n\omega_{\rm ph} + \omega_0)t] \begin{bmatrix} -\cos(\omega_0 t)E_{s,n_x} \\ -\sin(\omega_0 t)E_{s,n_y} \end{bmatrix}. \quad (7)$$

Now it is straightforward to notice that all the sidebands exhibit nonzero x and y components. The ellipticity and the phase difference are estimated from the nonzero components, and our numerical results shown in Fig. 6 are consistent with the present analysis. If a linearly polarized probe pulse is used instead of the circularly polarized pulse, the odd- and even-order sidebands are polarized perpendicular and parallel, respectively, to the polarization of probe pulse in the case of graphene with a M_{1x} phonon mode. On the other hand, the M_{2y} phonon mode leads to all sidebands being polarized along the direction of the probe pulse [45].

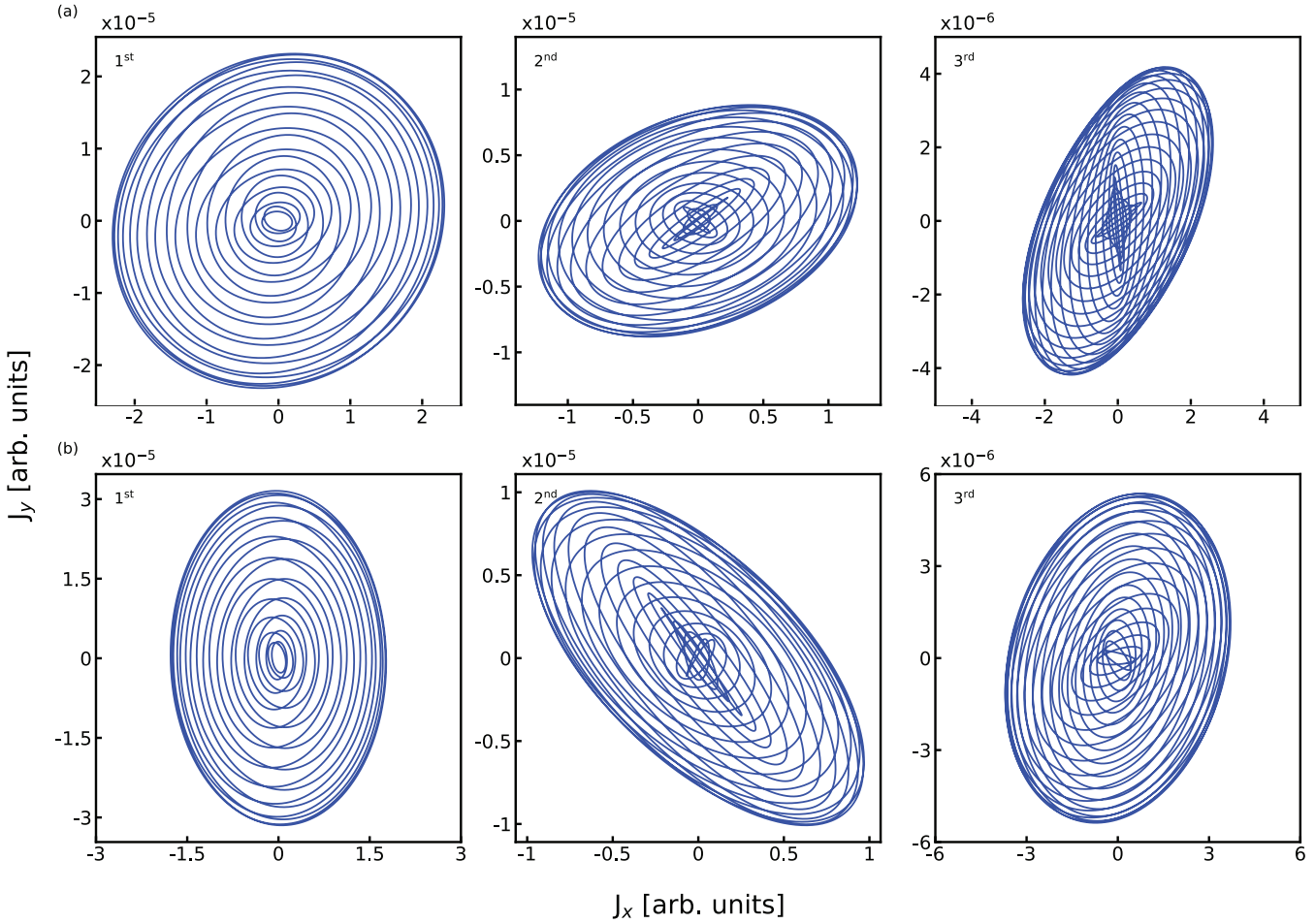

FIG. 6. Same as Fig. 4 for the first, second, and third sidebands associated with the first harmonic for graphene with (a) the M_{1x} phonon mode corresponding to Fig. 2(b) and (b) the M_{2y} phonon mode corresponding to Fig. 2(c). The ellipticities of the first, second, and third sidebands corresponding to the in-plane longitudinal optical (iLO) [in-plane transverse optical (iTO)] phonon mode are 0.98 (0.56), 0.72 (0.95), and 0.59 (0.67), respectively. The phase differences between x and y components of the first, second, and third sidebands corresponding to the M_{1x} (M_{2y}) phonon mode are 85° (90°), 70° (135°), and 60° (75°), respectively.

IV. CONCLUSION

In conclusion, we have explored the potential of high-order-harmonic spectroscopy in probing the effect of coherent phonon dynamics on electron dynamics in solids. To this end, coherent excitation of both in-plane M_{1x} and in-plane M_{2y} Raman-active phonon modes in graphene are considered. The sixfold symmetry of the graphene reduces to twofold dynamically due to the coherent phonon excitation. As a result of this symmetry alteration, the symmetry-forbidden third harmonic of the circularly polarized probe pulse is generated. Moreover, coherent phonon dynamics leads to the generation of the sidebands corresponding to the prominent harmonic peaks. The Floquet formalism of the dynamical symmetries of the system is applied to understand the properties of the sidebands. It is found that the positions of the sidebands are determined by the energy of the excited phonon modes. Moreover, the dynamical symmetries of the system, which consists of graphene with an excited phonon mode and probe pulse, determine the polarization of the sidebands. Thus polarization properties of the sidebands are a sensitive probe of the dynamical symmetries. The present study could be extended to bilayer graphene, where infrared-active phonon modes can be expressed in terms of double-degenerate in-plane Raman-active phonon modes of monolayer graphene [41,57].

ACKNOWLEDGMENTS

We acknowledge fruitful discussions with M. S. Mrudul (Uppsala University), Amber Jain (IIT Bombay), and Klaus Reimann (MBI Berlin). G.D. acknowledges support from Science and Engineering Research Board (SERB) India (Project No. MTR/2021/000138).

[1] W. Hu, S. Kaiser, D. Nicoletti, C. R. Hunt, I. Gierz, M. C. Hoffmann, M. Le Tacon, T. Loew, B. Keimer, and A. Cavalleri, Nat. Mater. **13**, 705 (2014).

[2] M. Mitrano, A. Cantaluppi, D. Nicoletti, S. Kaiser, A. Perucchi, S. Lupi, P. Di Pietro, D. Pontiroli, M. Riccò, S. R. Clark, D. Jaksch, and A. Cavalleri, Nature (London) **530**, 461 (2016).

[3] M. Rini, R. Tobey, N. Dean, J. Itatani, Y. Tomioka, Y. Tokura, R. W. Schoenlein, and A. Cavalleri, Nature (London) **449**, 72 (2007).

[4] T. F. Nova, A. Cartella, A. Cantaluppi, M. Först, D. Bossini, R. V. Mikhaylovskiy, A. V. Kimel, R. Merlin, and A. Cavalleri, Nat. Phys. **13**, 132 (2017).

[5] R. Mankowsky, A. von Hoegen, M. Först, and A. Cavalleri, Phys. Rev. Lett. **118**, 197601 (2017).

[6] D. Bansal, J. L. Niedziela, S. Calder, T. Lanigan-Atkins, R. Rawl, A. H. Said, D. L. Abernathy, A. I. Kolesnikov, H. Zhou, and O. Delaire, Nat. Phys. **16**, 669 (2020).

[7] M. Hase, P. Fons, K. Mitrofanov, A. V. Kolobov, and J. Tominaga, Nat. Commun. **6**, 8367 (2015).

[8] J. Niedziela, D. Bansal, A. May, J. Ding, T.L.-Atkins, G. Ehlers, D. Abernathy, A. Said, and O. Delaire, Nat. Phys. **15**, 73 (2019).

[9] D. Bansal, J. Niedziela, R. Sinclair, V. Garlea, D. Abernathy, S. Chi, Y. Ren, H. Zhou, and O. Delaire, Nat. Commun. **9**, 15 (2018).

[10] H. Katsuki, J. Delagnes, K. Hosaka, K. Ishioka, H. Chiba, E. Zijlstra, M. Garcia, H. Takahashi, K. Watanabe, M. Kitajima, Y. Matsumoto, K. G. Nakamura, and K. Ohmori, Nat. Commun. **4**, 2801 (2013).

[11] B. Fultz, Prog. Mater. Sci. **55**, 247 (2010).

[12] A. Gambetta, C. Manzoni, E. Menna, M. Meneghetti, G. Cerullo, G. Lanzani, S. Tretiak, A. Piryatinski, A. Saxena, R. Martin, and A. Bishop, Nat. Phys. **2**, 515 (2006).

[13] L. Dhar, J. A. Rogers, and K. A. Nelson, Chem. Rev. **94**, 157 (1994).

[14] T. Debnath, D. Sarker, H. Huang, Z.-K. Han, A. Dey, L. Polavarapu, S. V. Levchenko, and J. Feldmann, Nat. Commun. **12**, 2629 (2021).

[15] D. Graf, F. Molitor, K. Ensslin, C. Stampfer, A. Jungen, C. Hierold, and L. Wirtz, Nano Lett. **7**, 238 (2007).

[16] A. Virga, C. Ferrante, G. Batignani, D. De Fazio, A. Nunn, A. Ferrari, G. Cerullo, and T. Scopigno, Nat. Commun. **10**, 3658 (2019).

[17] J. Koivistoinen, P. Myllyperkio, and M. Pettersson, J. Phys. Chem. Lett. **8**, 4108 (2017).

[18] N. Rana, A. P. Roy, D. Bansal, and G. Dixit, npj Comput. Mater. **7**, 7 (2021).

[19] S. B. Brown, A. Gleason, E. Galtier, A. Higginbotham, B. Arnold, A. Fry, E. Granados, A. Hashim, C. G. Schroer, A. Schropp, F. Seiboth, F. Tavella, Z. Xing, W. Mao, H. Lee, and B. Nagler, Sci. Adv. **5**, eaau8044 (2019).

[20] D. J. Flannigan, Physics **11**, 53 (2018).

[21] S. Gerber, S.-L. Yang, D. Zhu, H. Soifer, J. Sobota, S. Rebec, J. Lee, T. Jia, B. Moritz, C. Jia, A. Gauthier, Y. Li, D. Leuenberger, Y. Zhang, L. Chaix, W. Li, H. Jang, J.-S. Lee, M. Yi, G. L. Dakovski *et al.*, Science **357**, 71 (2017).

[22] P. Hein, S. Jauernik, H. Erk, L. Yang, Y. Qi, Y. Sun, C. Felser, and M. Bauer, Nat. Commun. **11**, 2613 (2020).

[23] T. T. Luu, M. Garg, S. Y. Kruchinin, A. Moulet, M. T. Hassan, and E. Goulielmakis, Nature (London) **521**, 498 (2015).

[24] O. Schubert, M. Hohenleutner, F. Langer, B. Urbanek, C. Lange, U. Huttner, D. Golde, T. Meier, M. Kira, S. W. Koch, and R. Huber, Nat. Photon. **8**, 119 (2014).

[25] M. Mrudul, Á. Jiménez-Galán, M. Ivanov, and G. Dixit, Optica **8**, 422 (2021).

[26] M. S. Mrudul and G. Dixit, J. Phys. B: At. Mol. Opt. Phys. **54**, 224001 (2021).

[27] M. Hohenleutner, F. Langer, O. Schubert, M. Knorr, U. Huttner, S. W. Koch, M. Kira, and R. Huber, Nature (London) **523**, 572 (2015).

[28] B. Zaks, R.-B. Liu, and M. S. Sherwin, Nature (London) **483**, 580 (2012).

[29] A. Pattanayak, M. S. Mrudul, and G. Dixit, Phys. Rev. A **101**, 013404 (2020).

[30] F. Langer, C. P. Schmid, S. Schlauderer, M. Gmitra, J. Fabian, P. Nagler, C. Schüller, T. Korn, P. Hawkins, J. Steiner, U. Huttner, S. Koch, M. Kira, and R. Huber, Nature (London) **557**, 76 (2018).

[31] M. S. Mrudul, N. Tancogne-Dejean, A. Rubio, and G. Dixit, npj Comput. Mater. **6**, 10 (2020).

[32] T. T. Luu and H. J. Wörner, Nat. Commun. **9**, 916 (2018).

[33] H. B. Banks, Q. Wu, D. C. Valovcin, S. Mack, A. C. Gossard, L. Pfeiffer, R.-B. Liu, and M. S. Sherwin, Phys. Rev. X **7**, 041042 (2017).

[34] M. S. Mrudul, A. Pattanayak, M. Ivanov, and G. Dixit, Phys. Rev. A **100**, 043420 (2019).

[35] S. Imai, A. Ono, and S. Ishihara, Phys. Rev. Lett. **124**, 157404 (2020).

[36] M. Borsch, C. P. Schmid, L. Weigl, S. Schlauderer, N. Hofmann, C. Lange, J. T. Steiner, S. W. Koch, R. Huber, and M. Kira, Science **370**, 1204 (2020).

[37] A. Pattanayak, S. Pujari, and G. Dixit, Sci. Rep. **12**, 6722 (2022).

[38] J. S. Ginsberg, M. M. Jadidi, J. Zhang, C. Y. Chen, S. H. Chae, G. N. Patwardhan, L. Xian, N. Tancogne-Dejean, K. Watanabe, T. Taniguchi, J. Hone, A. Rubio, and A. Gaeta, arXiv:2107.11959.

[39] O. Neufeld, J. Zhang, U. D. Giovannini, H. Hübener, and A. Rubio, Proc. Natl. Acad. Sci. USA **119**, e2204219119 (2022).

[40] J.-H. Kim, A. Nugraha, L. Booshehri, E. Hároz, K. Sato, G. Sanders, K.-J. Yee, Y.-S. Lim, C. Stanton, R. Saito, and J. Kono, Chem. Phys. **413**, 55 (2013).

[41] I. Gierz, M. Mitrano, H. Bromberger, C. Cacho, R. Chapman, E. Springate, S. Link, U. Starke, B. Sachs, M. Eckstein, T. O. Wehling, M. I. Katsnelson, A. Lichtenstein, and A. Cavalleri, Phys. Rev. Lett. **114**, 125503 (2015).

[42] V. Mohanty and E. J. Heller, Proc. Natl. Acad. Sci. USA **116**, 18316 (2019).

[43] T. Ando, J. Phys. Soc. Jpn. **75**, 124701 (2006).

[44] P. Moon and M. Koshino, Phys. Rev. B **87**, 205404 (2013).

[45] N. Rana, M. S. Mrudul, D. Kartashov, M. Ivanov, and G. Dixit, Phys. Rev. B **106**, 064303 (2022).

[46] N. Tancogne-Dejean, O. D. Mücke, F. X. Kärtner, and A. Rubio, Nat. Commun. **8**, 745 (2017).

[47] K. Kang, D. Abdula, D. G. Cahill, and M. Shim, Phys. Rev. B **81**, 165405 (2010).

[48] N. Yoshikawa, T. Tamaya, and K. Tanaka, Science **356**, 736 (2017).

[49] O. E. Alon, V. Averbukh, and N. Moiseyev, Phys. Rev. Lett. **80**, 3743 (1998).

[50] Z. Y. Chen and R. Qin, Opt. Express **27**, 3761 (2019).

[51] O. Neufeld, D. Podolsky, and O. Cohen, Nat. Commun. **10**, 405 (2019).

[52] M. S. Mrudul and G. Dixit, Phys. Rev. B **103**, 094308 (2021).
[53] H. Hübener, U. De Giovannini, and A. Rubio, Nano Lett. **18**, 1535 (2018).
[54] N. Saito, P. Xia, F. Lu, T. Kanai, J. Itatani, and N. Ishii, Optica **4**, 1333 (2017).
[55] G. Vampa, C. R. McDonald, G. Orlando, P. B. Corkum, and T. Brabec, Phys. Rev. B **91**, 064302 (2015).
[56] K. Nagai, K. Uchida, N. Yoshikawa, T. Endo, Y. Miyata, and K. Tanaka, Commun. Phys. **3**, 137 (2020).
[57] M. Rodriguez-Vega, M. Vogl, and G. A. Fiete, Phys. Rev. B **104**, 245135 (2021).